AAS ASD-36 2490399

PERIODIC ORBIT-ATTITUDE SOLUTIONS IN THE PLANAR ELLIPTIC RESTRICTED THREE-BODY PROBLEM

Dayung Koh* **and Rodney L. Anderson†**

The pitch motion of a spacecraft in the planar elliptic restricted three-body system is studied. Previous studies laid the foundation for spacecraft stability analysis with a small perturbation to the zero pitch motion. In this study, a cell mapping approach that combines analytical and numerical techniques is used to study the global behavior of the full nonlinear spacecraft attitude in which coupling between orbital dynamics and attitude occurs. The effect of gravity gradient torques, orbital eccentricity, and the spacecraft configuration at different Lagrangian points is analyzed. Multiple-period periodic solutions and invariant surfaces are presented for different cases. Reference trajectories around the Lagrangian points are also considered to study coupled dynamics.

INTRODUCTION

The problem of gravity gradient satellites has been studied extensively in the two-body system. The classical studies on the topic were done by Beletskii[1] and Modi et al.[2] who formulated fundamental periodic solutions by employing the method of harmonic balance and boundary condition problems. Zlatoustov et al.[3] and Modi et al.[4] studied families of periodic solutions of the pitch oscillations by the method of numerical integration, and they investigated stability using a linear approximation. Koh and Flashner[5] investigated the pitch dynamics for elliptic orbits in the two-body problem using the cell mapping method, and rich nonlinear dynamic characteristics including multiple-period solutions, invariant surfaces, and bifurcations were found.

Recently, the success of libration orbit missions such as the International Sun-Earth Explorer-3[6] (ISEE-3), Genesis mission[7] (2001), and others[8] proved that the three-body problem can considerably enhance our ability to perform sophisticated scientific explorations. In the three-body problem, however, spacecraft experience complex dynamics that affect the gravity gradient torques in the coupled dynamics. Consequently, a fundamental understanding of the attitude motion in these complex dynamical environments is increasingly important.

The attitude dynamics in the three-body problem have not yet been fully discovered, although a variety of researchers have begun to study this problem. Kane and Marsh[9] and Robinson[10] showed the pitch motion stability chart for various configurations of a set of parameters at the libration points by employing linearized methods. Ashenberg[11] considered the elliptic three-body case and showed Poincaré maps and bifurcation diagrams for the nonlinear pitch dynamics for a dumbbell satellite at the libration points. Brucker and Gurfil[12] explored the dynamics using Poincaré maps

*Postdoctoral fellow, Jet Propulsion Laboratory, California Institute of Technology, 4800 Oak Grove Drive, M/S T1721-202E, Pasadena, CA 91109.

†Member of Technical Staff, Jet Propulsion Laboratory, California Institute of Technology, 4800 Oak Grove Drive, M/S 301-121, Pasadena, CA 91109.

with particular initial conditions focusing on the vicinity of the Lagrangian collinear points, and they also computed stability charts. Wong et al.[13] investigated stability characteristics of the small pitch motion but with spacecraft traveling in the linearly approximated orbits in the vicinity of libration points. Guzzetti and Howell[14] and Knutson et al.[15] investigated stability characteristics of the pitch motion using the Lyapunov and Halo orbit families. Most recently, Guzzetti and Howell[16] studied periodic solutions using Poincaré mapping, Floquet theory, and differential correctors. They noted that because of the complex dynamics, the formulation of periodic solutions depends significantly on the initial guess.

In this study, global periodic orbit-attitude dynamics of the pitch motion in the elliptic restricted three-body problem (ERTBP) are explored as we vary the spacecraft inertia parameter and the orbital eccentricity of the primaries. As other studies have noted, it is difficult to approach this problem using standard methods because of the coupled, nonlinear, and time-varying dynamics. One approach that is ideal for a numerical exploration of this problem is the cell mapping method[17,18] that is based on a combination of analytical and numerical techniques. Various extensions of the cell mapping method can be found, such as generalized cell mapping[19] using Markov chains and set oriented methods[20,21,22,23] using subdivision techniques. We are focused here on studying the global dynamical behavior of coupled nonlinear dynamics with a rapid and fundamental approach.

In the cell mapping approach (see Hsu[17]), the state variables are thought of as a collection of intervals. The cell state space S we are interested in is constructed by dividing each state variable component, θ and θ', into uniformly sized cells. In the cell state space S, a cell-to-cell mapping C is created. Solutions of period $K \cdot T$, where T is the system period 2π, are found when a cell repeats after applying the map K-times. An unravelling algorithm (see Hsu[18]) is used to find the periodic solutions.

The present paper is dedicated to analyzing the periodic orbit-attitude solutions in the ERTBP. The cell mapping method applied to the ERTBP will first be introduced, and then specific cases with varying parameters will be explored. Specifically, these cases will include 1) the two-body problem case compared to L_3 of the three-body problem, 2) L_2 and L_4 in the circular restricted three-body problem (CRTBP), 3) L_2 and L_4 in the ERTBP with varying orbital eccentricity and spacecraft inertia parameters, and 4) reference trajectories in the vicinity of L_2 and L_4.

PROBLEM DESCRIPTION

In this study, periodic orbit-attitude solutions are found in the ERTBP using a cell-mapping method. The motion of the spacecraft in the ERTBP is described in a rotating pulsating dimensionless frame, centered at the barycenter of M_1 (the primary) and M_2 (the secondary) as shown in Figure 1. The equations of motion for the attitude of an axi-symmetric rigid spacecraft acted upon by gravity gradient torques in the ERTBP is described by Euler's equations (see Hughes[24]):

$$\begin{aligned} I_1\,{}^I\dot{\omega}_1^B + (I_3 - I_2)\,{}^I\omega_3^B\,{}^I\omega_2^B &= g_1 \\ I_2\,{}^I\dot{\omega}_2^B + (I_1 - I_3)\,{}^I\omega_1^B\,{}^I\omega_3^B &= g_2 \\ I_3\,{}^I\dot{\omega}_3^B + (I_2 - I_1)\,{}^I\omega_2^B\,{}^I\omega_1^B &= g_3. \end{aligned} \tag{1}$$

Here, I_i is the moment of inertia of the spacecraft about the i-axis, ${}^I\omega_i^B$ denotes the i^{th} component of the body frame's angular velocity with respect to the inertial frame, and the gravitational torque,

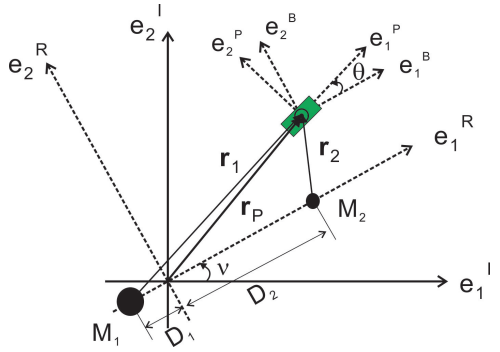

Figure 1. Geometry of a satellite in the ERTBP

g_i, induced by the primary and secondary bodies is given as

$$\begin{aligned}\bar{g} &= \frac{3M_1}{r^3 \cdot \rho_1^3}\hat{\rho}_1 \times I \cdot \hat{\rho}_1 + \frac{3M_2}{r^3 \cdot \rho_2^3}\hat{\rho}_2 \times I \cdot \hat{\rho}_2 \\ &= \frac{3M_1}{r^3 \cdot \rho_1^3}\begin{bmatrix} (I_3 - I_2)\hat{\rho}_{12}\hat{\rho}_{13} \\ (I_1 - I_3)\hat{\rho}_{13}\hat{\rho}_{11} \\ (I_2 - I_1)\hat{\rho}_{11}\hat{\rho}_{12} \end{bmatrix} + \frac{3M_2}{r^3 \cdot \rho_2^3}\begin{bmatrix} (I_3 - I_2)\hat{\rho}_{22}\hat{\rho}_{23} \\ (I_1 - I_3)\hat{\rho}_{23}\hat{\rho}_{21} \\ (I_2 - I_1)\hat{\rho}_{21}\hat{\rho}_{22} \end{bmatrix}\end{aligned} \tag{2}$$

where $\hat{\rho}_n$ denotes a unit vector from M_n to the center of the spacecraft in a pulsating rotating frame. By substituting Eq. (2) into Eq. (1), we get (see also Wong et al.[13])

$$\begin{aligned} I_1\,{}^I\dot{\omega}_1^B + (I_3 - I_2)\,{}^I\omega_3^B\,{}^I\omega_2^B &= \frac{3M_1}{r^3 \cdot \rho_1^3}(I_3 - I_2)\hat{\rho}_{12}\hat{\rho}_{13} + \frac{3M_2}{r^3 \cdot \rho_2^3}(I_3 - I_2)\hat{\rho}_{22}\hat{\rho}_{23} \\ I_2\,{}^I\dot{\omega}_2^B + (I_1 - I_3)\,{}^I\omega_1^B\,{}^I\omega_3^B &= \frac{3M_1}{r^3 \cdot \rho_1^3}(I_1 - I_3)\hat{\rho}_{13}\hat{\rho}_{11} + \frac{3M_2}{r^3 \cdot \rho_2^3}(I_1 - I_3)\hat{\rho}_{23}\hat{\rho}_{21} \\ I_3\,{}^I\dot{\omega}_3^B + (I_2 - I_1)\,{}^I\omega_2^B\,{}^I\omega_1^B &= \frac{3M_1}{r^3 \cdot \rho_1^3}(I_2 - I_1)\hat{\rho}_{11}\hat{\rho}_{12} + \frac{3M_2}{r^3 \cdot \rho_2^3}(I_2 - I_1)\hat{\rho}_{21}\hat{\rho}_{22}. \end{aligned} \tag{3}$$

Note that the pulsating frame is normalized using the distance r between M_1 and M_2,

$$\begin{aligned}\bar{r}_1 &= r \cdot \bar{\rho}_1 \\ \bar{r}_2 &= r \cdot \bar{\rho}_2\end{aligned} \tag{4}$$

where $r = \frac{1-e^2}{1+e\cos\nu}$. In Eq. (2), $\hat{\rho}_{1i}$ and $\hat{\rho}_{2i}$, i=1, 2, 3, represent the i^{th} component of the $\hat{\rho}_n$ vector. The position of the center of the spacecraft in the rotating frame [e^R] relative to its position vector, $\bar{r}_p$, can be written as

$$\bar{r}_1^R = \begin{bmatrix} x_p + D_1 \\ y_p \\ z_p \end{bmatrix}, \quad \bar{r}_2^R = \begin{bmatrix} x_p - D_2 \\ y_p \\ z_p \end{bmatrix} \tag{5}$$

where $\bar{r}_p$ is the position vector of the center of the spacecraft and D_n is the distance of the mass M_n from the barycenter in a dimensionless pulsating frame ($D_1 = \mu$ and $D_2 = 1 - \mu$, where $\mu = \frac{M_2}{M_1+M_2}$). The position vector in Eq. (5) can be written in the body frame as

$$\bar{r}_n^B = {}^BC^R \cdot \begin{bmatrix} x_p \pm D_n \\ y_p \\ z_p \end{bmatrix} \tag{6}$$

with '+' for $n = 1$, and '-' for $n = 2$, where

$$ {}^{B}C^{R} = \begin{bmatrix} c_\phi c_\theta & c_\phi s_\theta & -s_\phi \\ -c_\psi s_\theta + s_\psi s_\phi c_\theta & c_\psi c_\theta + s_\psi s_\phi s_\theta & s_\psi c_\phi \\ s_\psi s_\theta + c_\psi s_\phi c_\theta & -s_\psi c_\theta + c_\psi s_\phi s_\theta & c_\psi c_\phi \end{bmatrix}. \tag{7} $$

The body orientation is described in the body fixed frame, $\bar{e}^B$, with respect to the rotating frame, $\bar{e}^R$ using a 3-2-1 pitch, roll, and yaw (θ, ϕ, ψ) Euler rotation sequence. The corresponding body frame's angular velocity with respect to the inertial frame is

$$ \begin{aligned} {}^{I}\bar{\omega}^{B} &= {}^{I}\bar{\omega}^{R} + {}^{R}\bar{\omega}^{B} \\ &= {}^{B}C^{R} \begin{bmatrix} 0 \\ 0 \\ 1 \end{bmatrix} |\dot{\nu}| + \begin{bmatrix} 1 & 0 & -s_\phi \\ 0 & c_\psi & s_\psi c_\phi \\ 0 & -s_\psi & c_\psi s_\phi \end{bmatrix} \begin{bmatrix} \dot{\psi} \\ \dot{\phi} \\ \dot{\theta} \end{bmatrix} = \begin{bmatrix} -s_\psi |\dot{\nu}| + \dot{\psi} - s_\phi \dot{\theta} \\ s_\psi c_\phi |\dot{\nu}| + c_\psi \dot{\phi} + s_\psi c_\phi \dot{\theta} \\ c_\psi c_\phi |\dot{\nu}| - s_\psi \dot{\phi} + c_\psi c_\phi \dot{\theta} \end{bmatrix}. \end{aligned} \tag{8} $$

The spacecraft's displacement, $\bar{r}_p$, in Eq. (6) is prescribed in a cartesian coordinate system by

$$ \begin{aligned} {x_p}'' &= 2{y_p}' + \frac{r}{1-e^2}\left(x_p - (1-\mu)\frac{x_p+\mu}{\rho_1^3} - \mu\frac{x_p+\mu-1}{\rho_2^3} \right) \\ {y_p}'' &= -2{x_p}' + \frac{r}{1-e^2}\left(y_p - (1-\mu)\frac{y_p}{\rho_1^3} - \mu\frac{y_p}{\rho_2^3} \right) \\ {z_p}'' &= \frac{r}{1-e^2}\left(-(1-\mu)\frac{z_p}{\rho_1^3} - \mu\frac{z_p}{\rho_2^3} \right) \end{aligned} \tag{9} $$

where the prime denotes the derivative with respect to true anomaly. Euler's equations and the kinematic differential equations derived above are solved together by substituting Eqs. (4) - (9) to Eq. (3) to produce the orbit-attitude solutions of the spacecraft.

In this study, we consider pitch dynamics in the planar problem for which $\omega_1 = \omega_2 = 0$ and $\phi = \psi = 0$ which leaves only the last line in Eq. (3):

$$ I_3^I \dot{\omega}_3^B = \frac{3M_1}{r^3 \cdot \rho_1^3}(I_2 - I_1)\hat{\rho}_{11}\hat{\rho}_{12} + \frac{3M_2}{r^3 \cdot \rho_2^3}(I_2 - I_1)\hat{\rho}_{21}\hat{\rho}_{22}. \tag{10} $$

Using Eq. (8) and assuming planar motion gives

$$ {}^{I}\omega_3^B = \frac{d}{dt}(\theta + \nu). \tag{11} $$

The equations written with the true anomaly as the independent variable are more intuitive in the elliptic orbit problem. An independent variable transformation using the relationship

$$ \frac{d\nu}{dt} = \frac{(1 + e\cos\nu)^2}{\sqrt{(1-e^2)^3}} \tag{12} $$

leads to

$$
\begin{aligned}
{}^{I}\dot{\omega}_3^B &= \frac{d}{dt}(\dot{\theta}+\dot{\nu}) \\
&= \frac{d}{d\nu}\frac{d\nu}{dt}\left[\frac{d\theta}{d\nu}\frac{d\nu}{dt}+\frac{d\nu}{dt}\right] \\
&= \frac{d^2\theta}{d\nu^2}\left(\frac{d\nu}{dt}\right)^2+\frac{d\theta}{d\nu}\left(\frac{d}{d\nu}\frac{d\nu}{dt}\right)\frac{d\nu}{dt}+\left(\frac{d}{d\nu}\frac{d\nu}{dt}\right)\frac{d\nu}{dt} \\
&= \theta''\left(\frac{d\nu}{dt}\right)^2+(\theta'+1)\left(\frac{d}{d\nu}\frac{d\nu}{dt}\right)\frac{d\nu}{dt}
\end{aligned}
\tag{13}
$$

where the dot and the prime denotes the derivative with respect to time and ν, respectively.

By substituting Eq. (13) into Eq. (10) and using $r = \frac{1-e^2}{1+e\cos\nu}$ and $\hat{\rho}_n = \bar{\rho}_n/\rho_n$, we get

$$
\begin{aligned}
(1+e\cos\nu)\theta'' - 2e\sin\nu(\theta'+1) = {} & \frac{3\mu_1}{\rho_1^5}k_3[(y_p^2-(x_p+\mu)^2)\sin\theta\cos\theta+(x_p+\mu)y_p(\cos^2\theta-\sin^2\theta)] \\
& + \frac{3\mu_2}{\rho_2^5}k_3[(y_p^2-(x_p+\mu-1)^2)\sin\theta\cos\theta+(x_p+\mu-1)y_p(\cos^2\theta-\sin^2\theta)]
\end{aligned}
\tag{14}
$$

where $k_3 = (I_2 - I_1)/I_3$. The primaries' mass parameters using this notation are the same as the three-body problem, i.e. $M_1 = \mu_1 = 1-\mu$, and $M_2 = \mu_2 = \mu$. Example shapes of spacecraft for different inertia parameters k_3 are shown in Fig. 2.

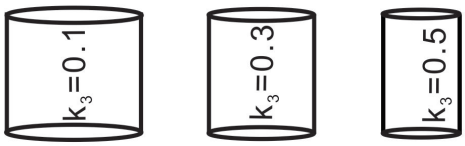

Figure 2. Example spacecraft shapes for different inertia parameters k_3

Note that for L_1, L_2, and L_3, this equation reduces to

$$
(1+e\cos\nu)\theta'' - 2e\sin\nu(1+\theta') = -\frac{3}{2}\left[\frac{1-\mu}{\rho_1^3}+\frac{\mu}{\rho_2^3}\right]k_3\sin 2\theta \tag{15}
$$

which is the same equation that Ashenberg[11] used in his study. For L_4 $(\frac{1}{2}-\mu, \frac{\sqrt{3}}{2})$ in the ERTBP, the equation becomes

$$
(1+e\cos\nu)\theta'' - 2e\sin\nu(1+\theta') = \frac{3}{4}\left[\sqrt{3}(1-2\mu)\cos 2\theta+\sin 2\theta\right]k_3. \tag{16}
$$

Note that with the flipped rotating frame with the primary at $(\mu, 0)$ and the secondary at $(-1+\mu, 0)$ used in Ashenberg,[11] the L_4 point is at $(-\frac{1}{2}+\mu, \frac{\sqrt{3}}{2})$ by his definition. Then the pitch motions at the L_4 point are mirror symmetric to the motions computed with the above equations of motion with respect to $x = 0$. For the case where $e = 0$, this reduces to the CRTBP, and Eq. (14) reduces to

$$
\begin{aligned}
\theta'' = \ddot{\theta} = {} & \frac{3\mu_1}{\rho_1^5}k_3[(y_p^2-(x_p+\mu)^2)\sin\theta\cos\theta+(x_p+\mu)y_p(\cos^2\theta-\sin^2\theta)] \\
& + \frac{3\mu_2}{\rho_2^5}k_3[(y_p^2-(x_p+\mu-1)^2)\sin\theta\cos\theta+(x_p+\mu-1)y_p(\cos^2\theta-\sin^2\theta)]
\end{aligned}
\tag{17}
$$

which is the same equation used in Knutson et al.[15]

METHODOLOGY

In this section, the cell mapping method of Hsu[17,18] and the extended cell mapping computation[27] are described. Thorough steps for analyzing global dynamic behavior using the methods with examples are introduced. In the final subsection, the computational implementation is summarized.

Cell mapping formulation

Consider a dynamical system

$$\dot{\boldsymbol{x}}(t) = f(t, \boldsymbol{x}(t)) \tag{18}$$

and define the states x_i, $i = 1, 2, ..., N$ (N=number of states) to get a state representation. The cell state space S is constructed by dividing the bounded state variables between $x_i^{(L)}$ (lower limit) and $x_i^{(U)}$ (upper limit) into a small interval with uniform size h_i. Each cell center is considered to be an entity represented by an integer, and the state space S is regarded as a collection of these cells. The region outside of this bounded region is defined as the 'sink cell.'

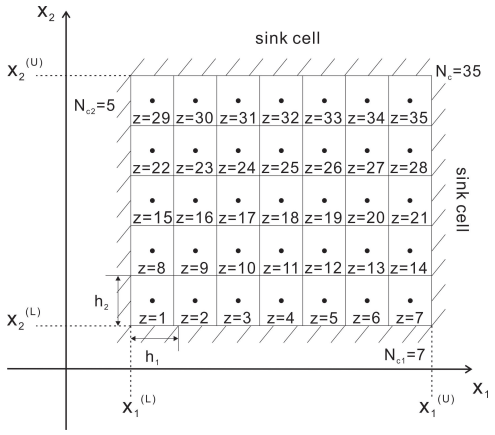

Figure 3. Cell state space for $N = 2$

Figure 3 presents an example for a two dimensional cell state space. Each state variable, x_1 and x_2, is divided into a finite number of cells, N_{c1} and N_{c2}, with intervals of h_1 and h_2, respectively. Then S contains a total number of cells $N_c = N_{c_1} \times N_{c_2} \times \cdots \times N_{c_N}$. Each cell is identified by its center point and numbered sequentially, $z = 1$ to $z = N_c$.

In the cell state space S, one can form the cell mapping C of a dynamical system by integrating it for one specified period T. The evolution of a discrete dynamical system can be described by

$$z(n+1) = C(z(n)) \tag{19}$$

where $C : S \to S,\ z(n) = 1, 2, \cdots, N_c$.

Table 1 gives an example of a schematic cell mapping with the cell state space shown in Fig. 3. Cells numbered from $z = 1$ to $z = 35$ are mapped to $C(z)$ after one integration of period T. The mapping $C(z) = 0$ indicates that cell z is mapped out of the cell state space to the sink cell. The cell z and mapping $C(z)$ can be stored as a vector form or a matrix form for the computational algorithm.

Table 1. Example of a cell mapping C(z)

z	C(z)	z	C(z)	z	C(z)	z	C(z)	z	C(z)
1	9	**8**	9	**15**	8	**22**	15	**29**	0
2	9	**9**	9	**16**	9	**23**	15	**30**	22
3	10	**10**	9	**17**	9	**24**	16	**31**	23
4	10	**11**	17	**18**	19	**25**	20	**32**	0
5	0	**12**	5	**19**	13	**26**	27	**33**	0
6	0	**13**	14	**20**	34	**27**	28	**34**	25
7	0	**14**	0	**21**	0	**28**	0	**35**	0

An intuitive understanding of the cell mapping may be obtained by observing the $C(z)$ in Table 1 in the cell state space, as shown in Figure 4. Arrows show the evolution of each center point after integration for one period.

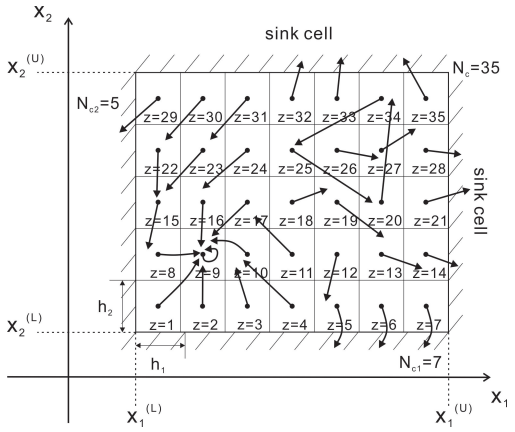

Figure 4. An example of cell mapping C(z)

Computation of discrete periodic solutions

Once the mapping process is complete, i.e., we have $C(z)$, the properties of the cells are determined using an unraveling algorithm (see Hsu[18]). The dynamics of the cell mapping is characterized by classifying singular cells as either equilibrium cells or periodic cells. An equilibrium (or period one) cell z^* is given by

$$z^* = C^1(z^*). \tag{20}$$

To define periodic cells, let C^m denote the cell mapping C applied m times (m is an integer) with C^0 understood to be the identity mapping. A sequence of K distinct cells $z^*(j)$, $j = 1, 2, \cdots, K$ which satisfies

$$\begin{aligned} z^*(m+1) &= C^m(z^*(1)),\ m = 1, 2, \cdots, K-1, \\ z^*(1) &= C^K(z^*(1)) \end{aligned} \tag{21}$$

is a $P-K$ mapping.

To delineate the global properties, three entities are defined from the unraveling algorithm, as follows:

1. Group number (Gr): Positive integers that are assigned sequentially as the periodic motions are discovered. Each group has an invariant set in the form of a periodic motion and shares the same periodicity number.

2. Periodicity number (P): This number indicates that the cell or a group that the cell belongs to is periodic with a period of $P \cdot T$.

3. Step number (S): The number of steps to map a cell into a group is assigned to each cell. If the step number of z is 0, it is a periodic cell.

Figure 5 shows some of the periodic cells for the previous mapping example (Fig. 4). The solid gray shaded cell is an equilibrium ($P-1$) cell which maps back to itself after one period. The

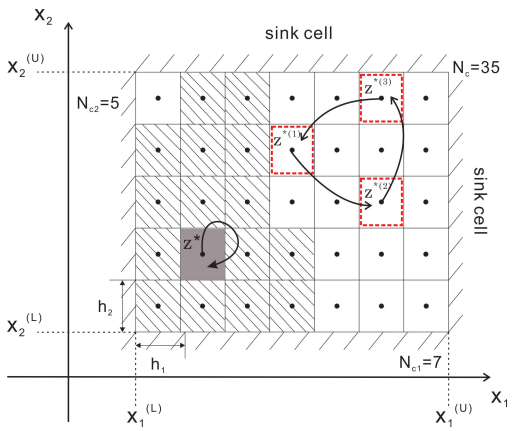

Figure 5. Equilibrium cell z^* and $P-K$ cells $z^{*(i)}$, $i=1,\cdots,K$ for $K=3$

red dashed edge cells ($z_{25} \rightarrow z_{20} \rightarrow z_{34} \rightarrow z_{25}$) are $P-3$ cells where each one of them maps back to the same cell after three periods. For further global dynamics analysis, the hatched cells are attracted to the cell $z=9$ (see the arrows in Fig. 4). White cells are the ones eventually mapped to the sink cell.

All of these dynamics characteristics can be determined by running the unraveling algorithm. The result of the unraveling algorithm is represented in another form in Table 2 based on the cell mapping example from Fig. 4 ($z=10$ to $z=19$ are omitted to save space). There are three groups: the $P-1$ solution (Gr = 1), the sink cell (Gr = 2), and the $P-3$ solution (Gr = 3). The same group number classifies types of motion sharing the same periodicity number. Note that the periodicity number for a sink cell is defined as 0. The unraveling algorithm runs sequentially from $z=1$ to $z=N_c$ until the algorithm reaches a periodic cell.

The unraveling algorithm starts with $z=1$ which maps to $z=9$. The cell $z=9$ maps to $z=9$ which is found to be a $P-1$ cell. Then the algorithm identifies the group and assigns the characteristic numbers for $z=1$ and 9 as Gr(1) =1, P(1)=1, S(1)=1 and Gr(9)=1, P(9)=1, S(9)=0. Then the algorithm moves on to $z=2$ which is the next unidentified cell, and it then maps to $z=9$

Table 2. Schematic cell mapping C(z)

z	C(z)	Gr	P	S	z	C(z)	Gr	P	S
1	9	1	1	1	**23**	15	1	1	3
2	9	1	1	1	**24**	16	1	1	2
3	10	1	1	2	**25**	20	3	3	0
4	10	1	1	2	**26**	27	2	0	3
5	0	2	0	1	**27**	28	2	0	2
6	0	2	0	1	**28**	0	2	0	1
7	0	2	0	1	**29**	0	2	0	1
8	9	1	1	1	**30**	22	1	1	4
9	9	1	1	0	**31**	23	1	1	4
...	...	...	...	...	**32**	0	2	0	1
20	34	3	3	0	**33**	0	2	0	1
21	0	2	0	1	**34**	25	3	3	0
22	15	1	1	3	**35**	0	2	0	1

again which was just defined as Gr(9)=1. Thus, it assigns the same group number and periodicity number as Gr(9) and P(9), i.e. Gr(2)=1, P(2)=1. The step number S(2) is 1 because it took one mapping to fall into the group. The next sequence follows with $z = 3$ until all the cells have been assigned group, periodicity, and step numbers.

In summary, the gray shaded $P - 1$ cell and the hatched cells in Figure 5 belong to the same group, Gr=1, sharing the same periodicity number, P=1. The white cells have Gr=2 and P=0. The dashed edge ones are $P - 3$ cells, and they are assigned Gr=3 and P=3.

Stability and bifurcation conditions

After finding a periodic solution $\boldsymbol{x}^*$, its local stability can be investigated using eigenvalues of the monodromy matrix. Let us define $\boldsymbol{u}(t) = \boldsymbol{x}(t) - \boldsymbol{x}^*(t; \boldsymbol{s})$ as the perturbation of the state $\boldsymbol{x}$ about a periodic solution $\boldsymbol{x}^*$. In order to analyze stability of the periodic solution, the system Eq. (18) is expressed as

$$\dot{\boldsymbol{u}}(t) = \boldsymbol{A}(t, \boldsymbol{s})\boldsymbol{u}(t) + \sum_{k=2}^{\infty} \boldsymbol{r}_k(t, \boldsymbol{u}(t), \boldsymbol{s}; \boldsymbol{x}^*), \tag{22}$$

where the matrix $\boldsymbol{A}(t) \in \boldsymbol{R}^{N \times N}$ is given by

$$\boldsymbol{A}(t, \boldsymbol{s}) = \left[\frac{\partial \boldsymbol{f}(t, \boldsymbol{x}, \boldsymbol{s})}{\partial \boldsymbol{x}} \right]_{x=x^*},$$

and $\boldsymbol{r}_k(t, \boldsymbol{u}(t), \boldsymbol{s}; \boldsymbol{x}^*)$ is a vector of all polynomials of degree k in the components of $\boldsymbol{u}(t)$.

Then a discrete-time representation expressed by time-invariant difference equations (see[25,26])

can be obtained as

$$\boldsymbol{u}_{m+1} = \boldsymbol{H}(\boldsymbol{s})\boldsymbol{u}_m + h.o.t,\ m = 1, 2, \cdots \tag{23}$$

where $H(\boldsymbol{s}) \in \boldsymbol{R}^{N\times N}$ is given by

$$\boldsymbol{H}(\boldsymbol{s}) = \boldsymbol{H}_K(\boldsymbol{s})\boldsymbol{H}_{K-1}(\boldsymbol{s})\cdots\boldsymbol{H}_1(\boldsymbol{s}). \tag{24}$$

Note that $\boldsymbol{H}(\boldsymbol{s})$ can be computed by using an algorithm for the computation of point mappings.[25,26]

The local stability of a $P-K$ solution is determined by the eigenvalues of matrix $\boldsymbol{H}(\boldsymbol{s})$. Note that for Hamiltonian systems, $\boldsymbol{H}$ is symplectic, i.e., $det\boldsymbol{H}(\boldsymbol{s}) = 1$ and all eigenvalues of $\boldsymbol{H}$ satisfy $\lambda_{i+1}(\boldsymbol{H}) = 1/\lambda_i(\boldsymbol{H})$. When the eigenvalues of $\boldsymbol{H}$ reside on the unit circle, the solution is locally stable. If not, the solution is unstable with the pairs of eigenvalues satisfying $|\lambda_i(\boldsymbol{H})| > 1$ and $|\lambda_{i+1}(\boldsymbol{H})| < 1$.

Bifurcation from a $P-K$ solution to a $P-MK$ solution may occur if there exists an integer M such that

$$det(\boldsymbol{I} - \boldsymbol{H}^M) = 0 \tag{25}$$

(see Flashner and Hsu[25]). In particular, one of the eigenvalues of $\boldsymbol{H}$ is $\lambda_{i,i+1} = 1$ for a $P-1$ to $P-1$ bifurcation, and $\lambda_{i,i+1} = -1$ for a $P-1$ to $P-2$ bifurcation.

Extended Cell Mapping Computation

Assume that cell $j_{1,2,3}$ are $P-3$ cells as shown in Fig. 6. Then the center of the cell $\boldsymbol{\phi}_j^*$ is mapped back to the same cell after three mapping iterations, i.e., $\boldsymbol{\phi}_j^* = \boldsymbol{G}^3(\boldsymbol{\phi}_j^*)$ when a discrete-time representation of the system $\dot{\boldsymbol{x}} = \boldsymbol{f}(t, \boldsymbol{x}(t), \boldsymbol{s})$ is formulated by an operator G,

$$\boldsymbol{x}_{n+1} = \boldsymbol{G}(\boldsymbol{x}_n, \boldsymbol{s}),\ n = 1, 2, \cdots . \tag{26}$$

However, the center of the cell $\boldsymbol{\phi}_j^*$ may not be an exact $P-3$ point. We called it as a 'discrete periodic solution' from the cell mapping. The exact periodic point can be another location in the vicinity of the center point. We shall use the concept of extended cell mapping introduced by Golat et al.[27] to develop an algorithm for computing the exact periodic point $\boldsymbol{z}^*$ with a parameter ζ.

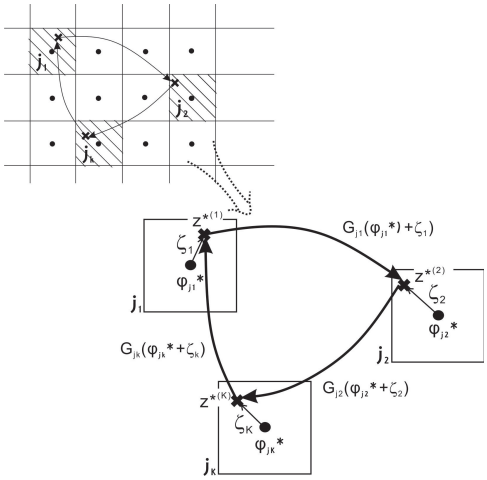

Figure 6. Illustration of the extended cell mapping method

For a general argument, assume that cells $j_1, \cdots, j_K$ constitute $P-K$ solutions which hold the following sequence of mappings:

$$\boldsymbol{\phi}^*_{j_1} \xrightarrow{\boldsymbol{G}(\boldsymbol{\phi}^*_{j_1})} \boldsymbol{\phi}^*_{j_2} \xrightarrow{\boldsymbol{G}(\boldsymbol{\phi}^*_{j_2})} \cdots \boldsymbol{\phi}^*_{j_K} \xrightarrow{\boldsymbol{G}(\boldsymbol{\phi}^*_{j_K})} \boldsymbol{\phi}^*_{j_1}$$

where $\boldsymbol{\phi}^*_{j_i}$ is the center of the cell $j_i,\ i = 1, \cdots, K$. The exact $P-K$ solutions are at locations $\boldsymbol{\zeta}_i$ from the center of the periodic cells $\boldsymbol{\phi}^*_{j_i}$, $i = 1, \cdots, K$, as shown in Fig. 6. Then the perturbation of the center of cells, $\boldsymbol{\zeta}_i$, satisfies the following sequence of point mapping

$$\begin{aligned} \boldsymbol{G}(\boldsymbol{\phi}^*_{j_i} + \boldsymbol{\zeta}_i) &= \boldsymbol{\phi}^*_{j_{i+1}} + \boldsymbol{\zeta}_{i+1},\ i = 1, \cdots, K-1 \\ \boldsymbol{G}(\boldsymbol{\phi}^*_{j_K} + \boldsymbol{\zeta}_K) &= \boldsymbol{\phi}^*_{j_1} + \boldsymbol{\zeta}_1. \end{aligned} \tag{27}$$

We have $N \cdot K$ equations with $N \cdot K$ unknowns where N is the number of states.

Expansion of the function $\boldsymbol{G}$ in Eq. (27) in Taylor series about the solution $\boldsymbol{\phi}^*_j$ yields

$$\boldsymbol{G}(\boldsymbol{\phi}^*_{j_i} + \boldsymbol{\zeta}_i) = \boldsymbol{G}(\boldsymbol{\phi}^*_{j_i}) + \boldsymbol{G}_{(m)}(\boldsymbol{\zeta}_i),\ i = 1, \cdots, K. \tag{28}$$

The value of $\boldsymbol{G}(\boldsymbol{\phi}^*_{j_i})$ can be obtained by integration of the continuous-time equations given in Eq. (18) over one period of time with initial conditions $\boldsymbol{x}(0) = \boldsymbol{\phi}^*_{j_i}$ and substitution of Eq. (28) into Eq. (27) yields:

$$\begin{aligned} \boldsymbol{\zeta}_{i+1} &= \boldsymbol{G}(\boldsymbol{\phi}^*_{j_i}) - \boldsymbol{\phi}^*_{j_{i+1}} + \boldsymbol{G}_{(m)}(\boldsymbol{\zeta}_i),\ i = 1, \cdots, K-1 \\ \boldsymbol{\zeta}_1 &= \boldsymbol{G}(\boldsymbol{\phi}^*_{j_K}) - \boldsymbol{\phi}^*_{j_1} + \boldsymbol{G}_{(m)}(\boldsymbol{\zeta}_K). \end{aligned} \tag{29}$$

For $m = 1$, i.e., the linear approximation of Eq. (29) takes the form

$$\begin{aligned} \boldsymbol{\zeta}_{i+1} &= \triangle_i + \boldsymbol{H}_i \cdot \boldsymbol{\zeta}_i \\ \boldsymbol{\zeta}_1 &= \triangle_K + \boldsymbol{H}_K \cdot \boldsymbol{\zeta}_K \end{aligned} \tag{30}$$

where

$$\begin{aligned} \triangle_i &= \boldsymbol{G}(\boldsymbol{\phi}^*_{j_i}) - \boldsymbol{\phi}^*_{j_{i+1}},\ i = 1, \cdots, K-1, \\ \triangle_K &= \boldsymbol{G}(\boldsymbol{\phi}^*_{j_K}) - \boldsymbol{\phi}^*_{j_1}, \quad \boldsymbol{H}_i = \left[\frac{\partial \boldsymbol{G}}{\partial \boldsymbol{x}}\right]_{\boldsymbol{\phi}^*_{j_i}}. \end{aligned}$$

Thus, the correction $\boldsymbol{\zeta}_1$ can be found iteratively with the first point of the $P-K$ solution, and $\boldsymbol{\zeta}_1$ is

$$(\boldsymbol{I} - \boldsymbol{H})\boldsymbol{\zeta}_1 = \boldsymbol{b} \implies \boldsymbol{\zeta}_1 = (\boldsymbol{I} - \boldsymbol{H})^{-1}\boldsymbol{b} \tag{31}$$

where $\boldsymbol{H} = \prod_{i=1}^{K} \boldsymbol{H}_i$, $\boldsymbol{b} = \triangle_K + \sum_{i=1}^{K-1}(\prod_{K=i+1}^{K} \boldsymbol{H}_K) \cdot \triangle_i$. Note that Eq. (31) has a singularity problem if we are at a bifurcation point. The rest of the corrections, $\boldsymbol{\zeta}_i$, $i = 2, \cdots,\ K$, are computed using Eq. (30).

Cell mapping implementation

For the global analysis of the nonlinear dynamic system, the cell mapping method is utilized. Two main steps for the global analysis are developed. First, the cell mapping is obtained for the given dynamical system by integrating over one desired period T. Then, the global properties, such as equilibrium points, discrete multiple-period periodic solutions, and regions of attraction of the system are extracted by an unraveling algorithm.

The computational algorithm is written using the MATLAB parallel computing tool box and implemented on a high performance computation (HPC) supercomputer for better computational performance. A procedure for the study is summarized in the following.

1. Select a cell state space and divide it into a finite number of cells as in Fig. 3.
2. Develop a cell mapping for the state space, see Eq. (19), Table 1, and Fig. 4.
3. Employ the unraveling algorithm (see Hsu[18]) to analyze global properties, see Fig. 5 and Table 2.
4. Run the extended cell mapping method to increase the accuracy of the discrete $P-K$ solutions found in Step 3, see Eq. (27).
5. Evaluate the local stability characteristics and bifurcation conditions of each solution using eigenvalues of the monodromy matrix of Eq. (24).

RESULTS

The two body problem vs. CRTBP at L_3

To begin the study of the complex nonlinear spacecraft attitude coupled with orbital dynamics in the three-body problem, one of the cases of a gravity gradient satellite in the two-body system study[5] is recalled as shown in Figure 7a. The assumption of only one primary (such as the Earth) exerting a gravitational influence on an orbiting satellite was made, and the system is non-dimensionalized. The present investigation involves studying the effect of the two primaries (such as the Earth and the Moon) on the attitude behavior of the spacecraft. To facilitate discussion of the comparison, the spacecraft is located at L_3 where it is farthest from the second primary's gravitational effect.

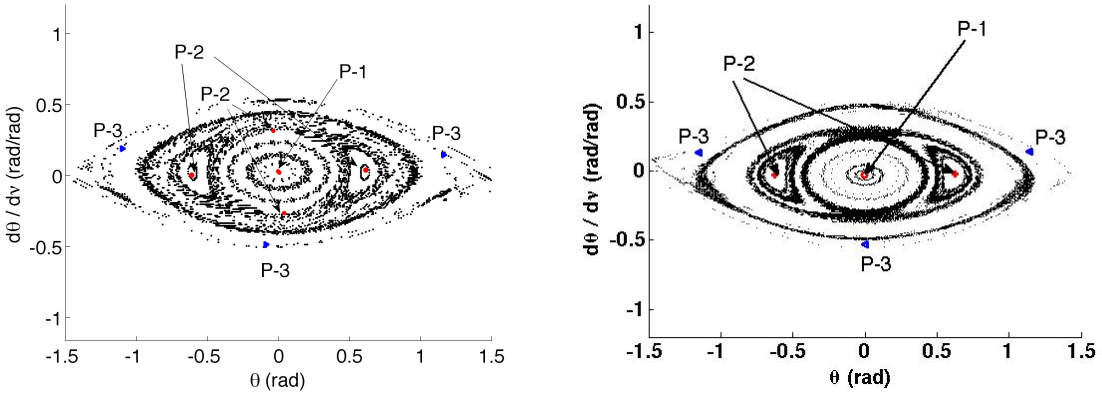

(a) The two-body system[5]

(b) The elliptic restricted three-body problem, L_3

Figure 7. Cell mapping results for the two-body problem and the ERTBP at L_3 of the Earth-Moon system, $k_3 = 0.1$, $e = 0.01$

The cell mapping results showing the discrete periodic solutions for the pitch motion of a spacecraft located at L_3 with $k_3 = 0.1$ and $e = 0.01$ are shown in Figure 7b. For this case, the position of the spacecraft was known to be at the L_3 equilibrium point in the ERTBP at all times. The cell mapping grid was set up in $[\theta, \theta']$ with an interval size of 0.005 radians (0.2865 deg) in θ and 0.005 radian/radian (0.2865 deg/rad) in θ'. The cell map was computed at a period of 2π, and the resulting $P-K$ solutions were found using the unraveling algorithm. The $P-1$, $P-2$, and $P-3$ periodic solutions from this analysis are shown in Figure 7b as well as islands of points around these

solutions. The islands are points corresponding to selected solutions with the same group number, chosen to illustrate overall attitude dynamics in the region.

Comparison of the cell mapping results in Figure 7 shows that the attitude dynamics for the two cases have nearly identical patterns. Kane and Marsh[9] mentioned this similarity using the stability chart. The center point of the invariant curves is the $P-1$ solution. Both have stable behavior with the spacecraft initially pointing to the first primary (or the only primary, the Earth) with small initial θ' such as $\theta'|_{twobody} = 0.028337\ rad/rad$ $(1.6236\ deg/rad)$ and $\theta'|_{L_3} = -0.029416\ rad/rad$ $(-1.6854\ deg/rad)$. The similarity is found for the $P-2$ and $P-3$ solutions and its invariant surface as well. Note that the same configuration ($e = 0.01$ and $k_3 = 0.1$) dynamics was studied at L_2 and L_4 and presented in Figure 13a and Figure 26a, respectively. The loss of the similarity at L_2 and L_4 can be attributed to the fact that the second primary's gravity field significantly affects the attitude dynamics.

CRTBP at L_2 and L_4, $k_3 = 1$

Ashenberg[11] used bifurcation diagrams and Poincaré maps to explore periodic motions with dumbbell shaped spacecraft ($k_3 = 1$) located at L_2 and L_4 of the Earth-Moon system ($T = 2\pi$) while assuming the eccentricity is zero with zero initial state. The study presented Poincaré maps with $P-1$, $P-2$, and $P-3$ solutions. Here, the study is repeated using the cell mapping method, verifying the existence of pendulum-like periodic solutions.

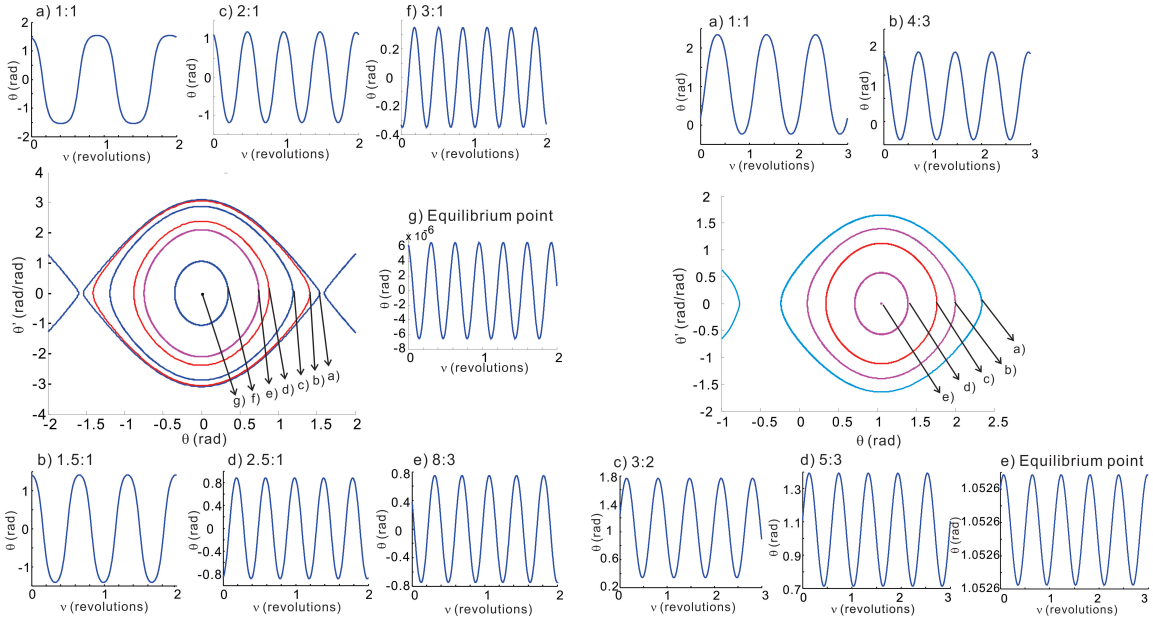

(a) L_2 (b) L_4

Figure 8. Cell mapping results for $T = 2\pi$ (in the middle) and pitch dynamics vs. true anomaly at the Lagrangian points of the Earth-Moon system, $k_3 = 1$, $e = 0$

The cell mapping results are shown in the middle of Figure 8 for both cases. Each point on the curves represents an initial condition for periodic motion with a period of 2π, the mapping period. One of the solutions was selected from each curve to show its motion over two-orbital revolutions

(θ vs. ν). The periodic motions with different frequency responses, m:n, are presented where m and n are the number of pitch librations and the number of orbits of the spacecraft, respectively. The outermost curve, a), for both is a $P-1$ solution, and the ratio increases as the pitch amplitude decreases in size. The center point in Figure 8 for both cases is an equilibrium point. The spacecraft orientation with the equilibrium pitch state $\theta_0|_{L2} = 0$ and $\theta_0|_{L4} = 60.3070$ deg with $\theta' = 0$ is shown in Figure 9. The stable solution shown in Figure 9 corresponds to the case where the spacecraft attitude initially points to the Earth. In this case, the spacecraft remains in this orientation across time at the libration point. Note that this case is addressed again in the later sections to investigate how the orbital eccentricity affects the pitch motion.

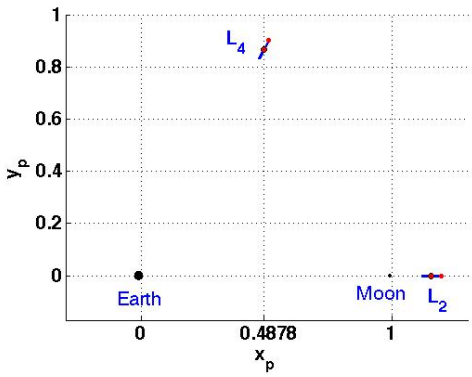

Figure 9. Equilibrium pitch motion at L_2 and L_4 for $e = 0$

It is interesting to explore the case where the eccentricity of the primaries is varied, and the Earth-Moon system with $e \approx 0.05$ is one realistic case of interest. Figure 10 shows the effect of the primaries' orbital eccentricity on the pitch motion of a spacecraft placed at L_4 using the cell mapping method. An isolated unstable $P-1$ solution appears for $e = 0.05$ (see Figure 10a). As

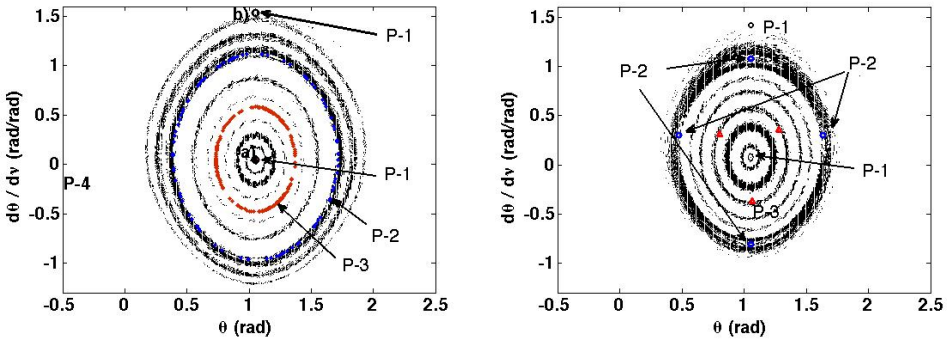

(a) L_4, $e = 0.05$ (b) L_4, $e = 0.1$

Figure 10. Cell mapping for $T = 2\pi$ at the Lagrangian point L_4 of the Earth-Moon system including eccentricity, $k_3 = 1$.

orbital eccentricity is increased, $P-2$ and $P-3$ solutions with invariant surfaces around them are also found using the cell mapping algorithm. Figure 10b shows two islands around a stable $P-2$

solution. Another $P-2$ solution predicted from the cell mapping is shown. Triangles indicate the possible existence of $P-3$ solutions from the cell mapping step. The accuracy of the solutions from the cell mapping (discrete periodic solutions) may be updated by running the extended cell mapping, and future work will focus on refining these solutions further. The cell mapping solutions (discrete periodic solutions) are run to a tolerance of approximately 0.001 radians, since the grid used for the cell mapping was from 0.001 to 0.005. The refined $P-1$ states with the extended cell mapping step a) $(60.3038$ deg, 2.5554 deg/rad$)$ and $(60.3153$ deg, 87.9433 deg/rad$)$ at $e=0.05$ are shown in Fig. 11. The initial orientation is close to the equilibrium condition at $e=0$, but it has a pitch velocity that maintains attitude. The corresponding trajectories in the phase plane and the angular response with the true anomaly for selected points are shown in Figure 12, verifying their periodicity.

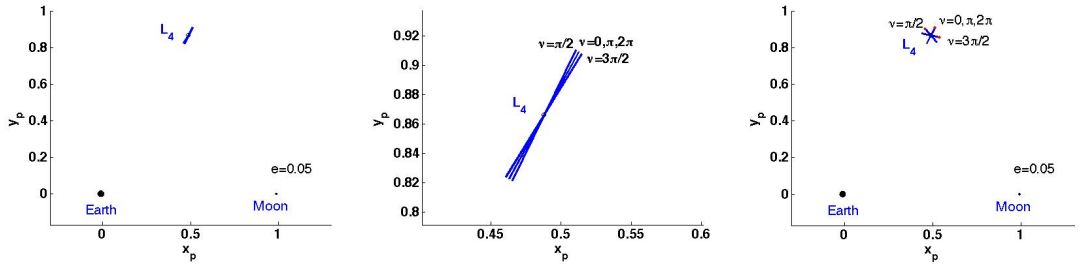

(a) $(\theta,\theta')|_0$=(1.0525 0.0446) (b) closer view of (a) (c) $(\theta,\theta')|_0$=(1.0527 1.5349)

Figure 11. Example of $P-1$ pitch motion at L_4 of the Earth-Moon system, $k_3=1$

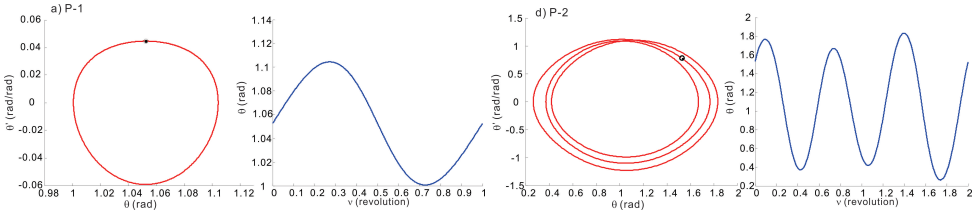

(a) L_4, $e=0.05$ a) P-1 (b) L_4, $e=0.05$ d) P-2

Figure 12. Pitch dynamics at the Lagrangian point L_4 of the Earth-Moon system including eccentricity, $k_3=1$

ERTBP at L_2 and CRTBP reference trajectories around $L_{1,2}$

The effect of the two primaries' gravity gradient torques, orbital eccentricity, and shape of the spacecraft on the pitch motion of the spacecraft when the spacecraft is placed at L_2 is studied. First, k_3 is fixed as 0.1 with varying orbital eccentricity, and e is fixed as 0.05 with varying k_3 while the spacecraft is located at L_2. Next, some Lyapunov orbits were considered as reference trajectories. Global pitch dynamic behavior including invariant surfaces, multiple-periodic solutions, and bifurcations which were not previously known are revealed.

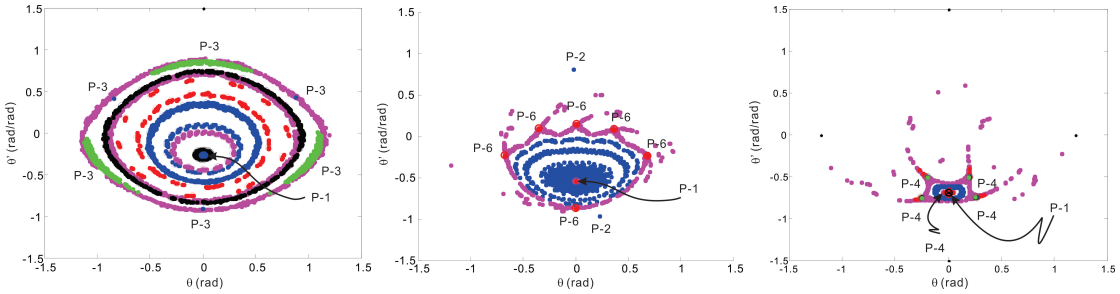

(a) $e = 0.01$ (b) $e = 0.05$ (c) $e = 0.1$

Figure 13. Cell mapping for $T = 2\pi$ at L_2 in the ERTBP, $k_3 = 0.1$

Varying eccentricity at L_2, $k_3 = 0.1$ Since most studies have focused on the circular case or linearized solutions,[11] it is important to explore how the primaries' orbital eccentricity affects the pitch motion. For that, the inertia parameter k_3 is fixed as 0.1 (see Fig. 2), and the invariant surfaces are found for varying orbital eccentricity using the cell mapping method. As shown in Fig. 13, the islands around the $P-1$ solution and discrete multiple-period solutions have been found. The amplitude of $P-1$ motion increases in size as the orbital eccentricity increases but the size of the invariant surface shrinks.

To better understand the invariant surfaces from the unraveling algorithm, different groups are broken down into steps for the case $e = 0.05$. Selected groups labeled sequentially are shown in Fig. 14. Each group represents a different period of the invariant surface, and the attitude motion is bounded within the corresponding initial conditions. In Fig. 14c, group 3 contains $P-6$ solutions, and Fig. 14l, or group 12, is a group of $P-1$ solutions.

The equilibrium solution at $(0, 0)$ no longer exists for these eccentric orbits, and the $P-1$ motion with some value of initial pitch velocity exists as shown in Fig. 15 in the phase plane. As orbital eccentricity is increased, a larger initial θ' is required to maintain the position pointing to the Moon at $\nu = 0$. These $P-1$ solutions have a tolerance of approximately $2e-5$ radians. To show the effect of the eccentricity, the pitch motion with the $(0, 0)$ initial condition is compared to the $P-1$ solution's initial condition for $7 \cdot T$ at $e = 0.01$. Figures 16b and 16d show the phase plane with the initial condition, and 16a and 16c indicate the corresponding pitch motion in the rotating frame captured every period for seven orbital revolutions. The body coordinate frame e_1^B (solid line) and e_2^B (dashed line) is placed at L_2. Note that the spacecraft is in planar motion, i.e., z_p and e_3^B are in the out of plane direction, and the body frame is not to scale. The spacecraft maintains its attitude with the $P-1$ solution at periapsis found from the cell mapping, whereas the pitch motion amplitude continuously grows as ν increases for the case with an initial condition at $(0, 0)$.

Multiple-period solutions which might be useful for various scenarios of pointing at different locations are found as well using the cell mapping method. As an example, the $P-6$ solution at $e = 0.05$ is presented in the phase plane in Figure 17. The extended cell mapping can be applied to multiple-periodic solutions updating and refining each point in parallel. The tolerance of the $P-6$ solution was tightened down to $1e-4$ radians. Note that the reference point/trajectory was fixed as initially set at all times.

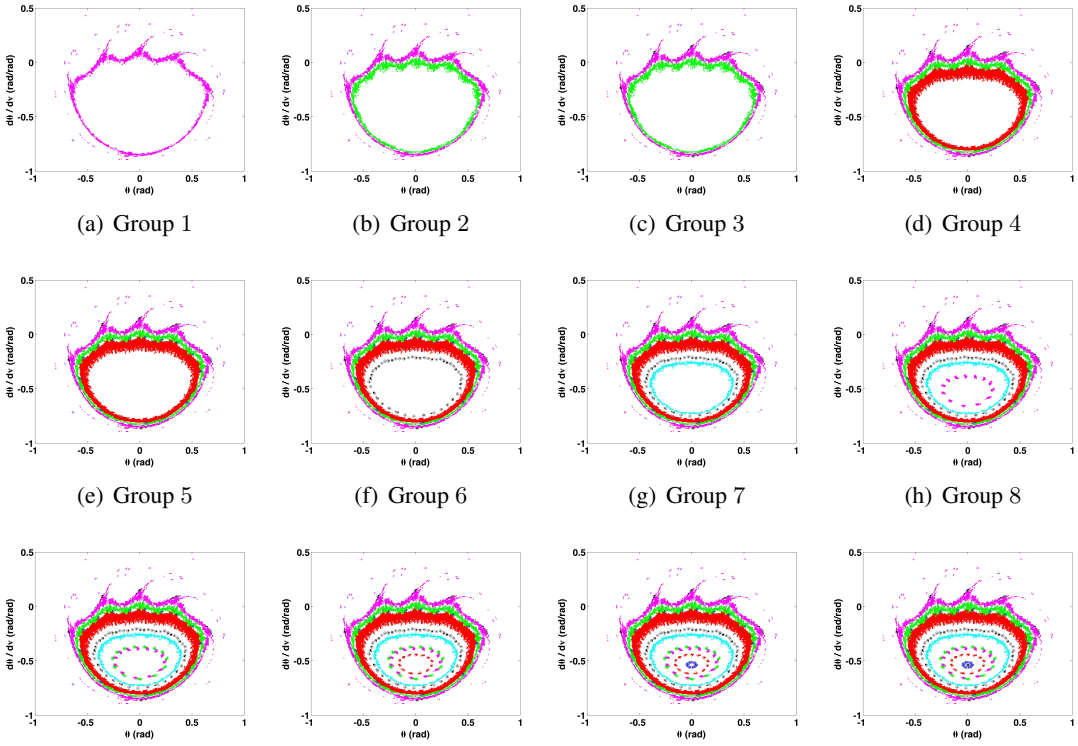

(a) Group 1 (b) Group 2 (c) Group 3 (d) Group 4

(e) Group 5 (f) Group 6 (g) Group 7 (h) Group 8

(i) Group 9 (j) Group 10 (k) Group 11 (l) Group 12

Figure 14. Selected groups from the unraveling algorithm, $e = 0.05$

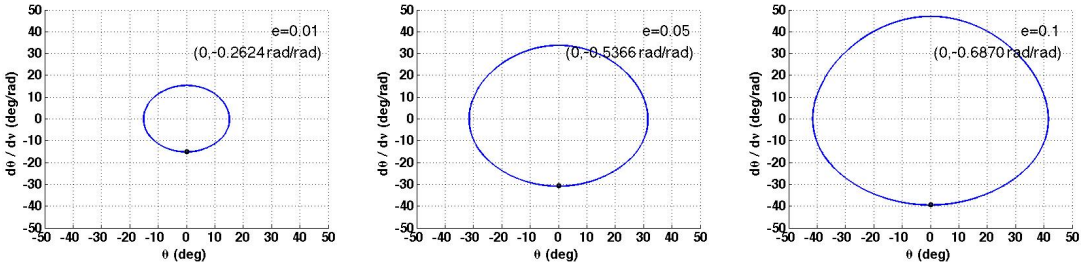

(a) $e = 0.01$ (b) $e = 0.05$ (c) $e = 0.1$

Figure 15. Pitch vs. Pitch velocity of $P - 1$ **solution,** $k_3 = 0.1$

Varying inertia parameter at L_2, $e = 0.05$ It is also interesting to study the pitch dynamics with a varying spacecraft inertia parameter. The orbital eccentricity is chosen as $e = 0.05$ for the Earth-Moon ERTBP, and pitch dynamics is studied at L_2. One to three $P-1$ solutions at $\theta_0 = 0$ are found, and invariant surfaces around them are discovered for different k_3 as shown in Figure 18. Multiple-periodic solutions such as $P - 2$ and $P - 3$ are found as well. The potential $P - 3$ solutions from the cell-mapping step are shown in Figure 18a, and further refinement can then be applied to find the periodic solutions using a stricter tolerance.

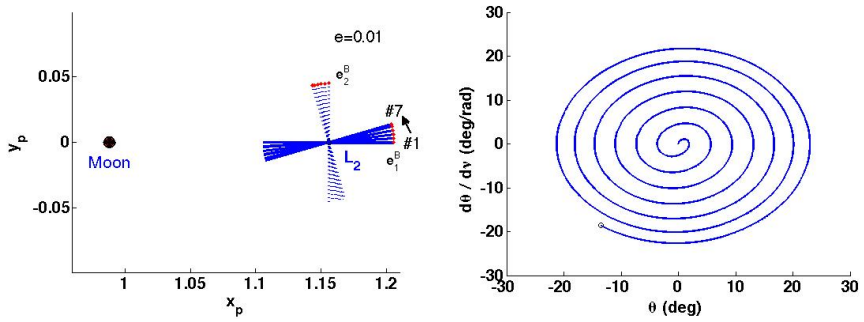

(a) $e = 0.01$, (0,0) at every $\nu = 0$ (b) $e = 0.01$, (0,0) for $7 \cdot T$

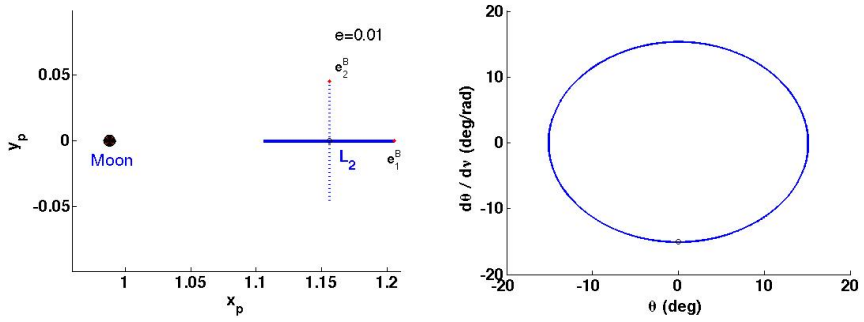

(c) $e = 0.01$, $P - 1$ at every $\nu = 0$ (d) $e = 0.01$, $P - 1$ for $7 \cdot T$

Figure 16. Pitch motion captured every period for 7 orbital revolutions $\nu = 0$ comparing initial conditions of $(0, 0)$ and $P - 1$, $e = 0.01$

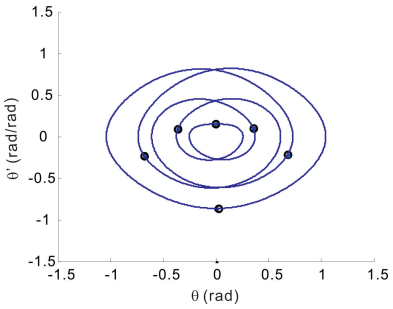

Figure 17. $P - 6$ solution trajectory in the phase plane

The $P - 1$ solutions found using the cell mapping method can be shown in a bifurcation diagram as presented in Fig. 19. There is one stable $P - 1$ solution for $k_3 = 0.1$. An unstable $P - 1$ solution and a stable $P - 1$ solution evolves near $k_3 = 0.15$.

It is demonstrated how spacecraft ($k_3 = 0.3$) behave throughout each orbital revolution for two of the $P - 1$ solutions, $P - 1$ (a) and $P - 1$ (b) in Fig. 20. As expected, $P - 1$(a) maintains its pitch angle close to zero. $P - 1$(b) oscillates with a larger angle about zero, but comes back to the initial condition after one period. $P - 2$ motion is shown in Fig. 21. The pitch motion starts at '1)' as an initial condition, passes '2)', and comes back to the initial attitude condition at $2 \cdot T$. The

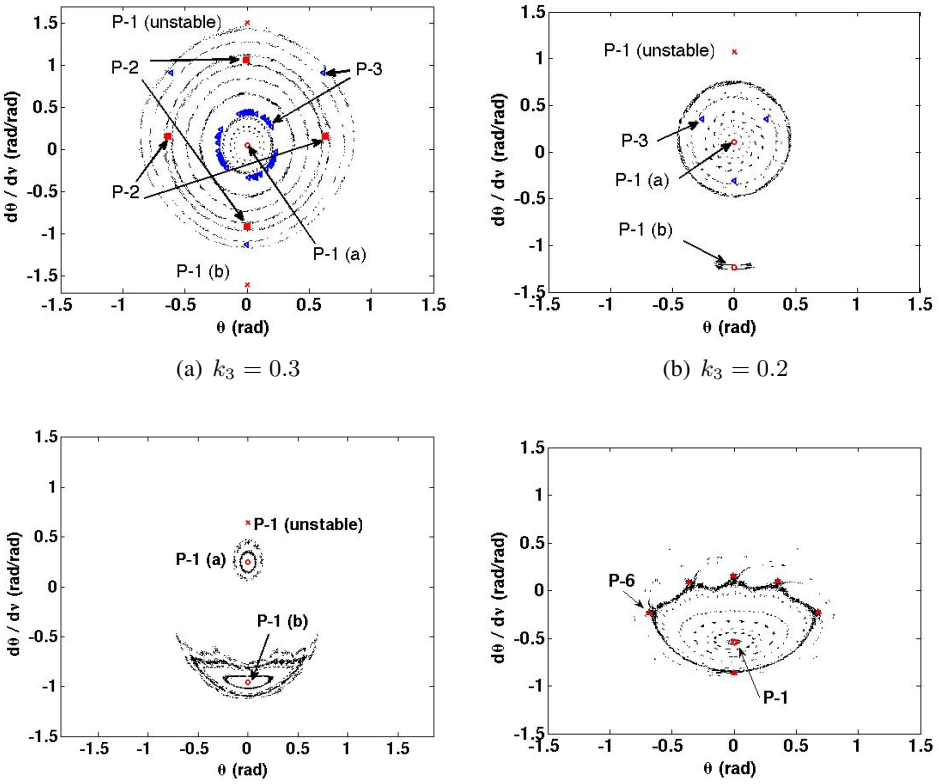

(a) $k_3 = 0.3$ (b) $k_3 = 0.2$

(c) $k_3 = 0.15$ (d) $k_3 = 0.1$

Figure 18. Cell mapping for $T = 2\pi$ at L_2 in the ERTBP, $e = 0.05$

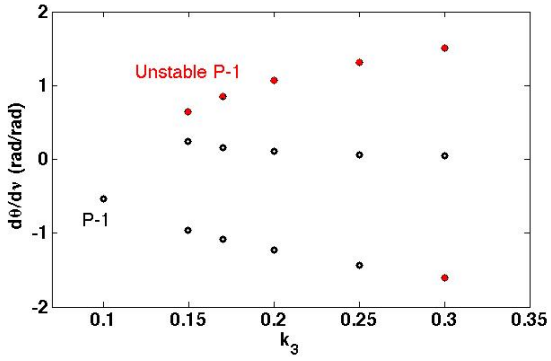

Figure 19. Bifurcation diagram $d\theta/d\nu$ vs k_3

corresponding pitch motion is shown in the rotating frame in Fig. 21a. Again, the body coordinate frame e_1^B (solid line) and e_2^B (dashed line) is placed at L_2.

CRTBP reference trajectories around $L_{1,2}$ Now that the pitch dynamics at L_2 have been explored, it is interesting to analyze how the motion translates when the spacecraft is placed on reference trajectories. Three Lyapunov orbits were chosen to show in this paper, a Lyapunov orbit around L_1

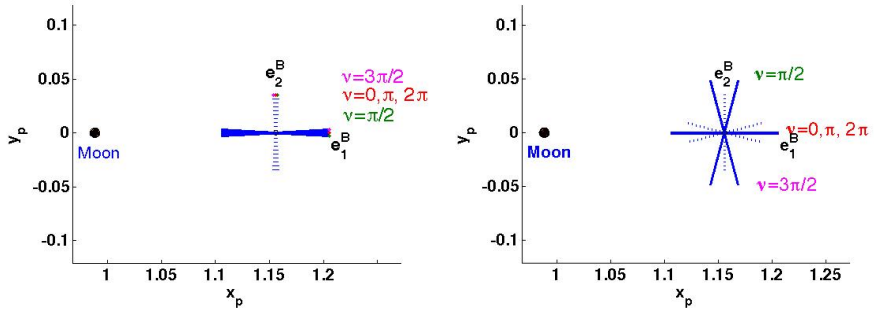

(a) $P-1$ (a), $k_3 = 0.3$ (b) $P-1$ (b), $k_3 = 0.3$

Figure 20. Pitch motion of $P-1$ at L_2 in the ERTBP, $e = 0.05$

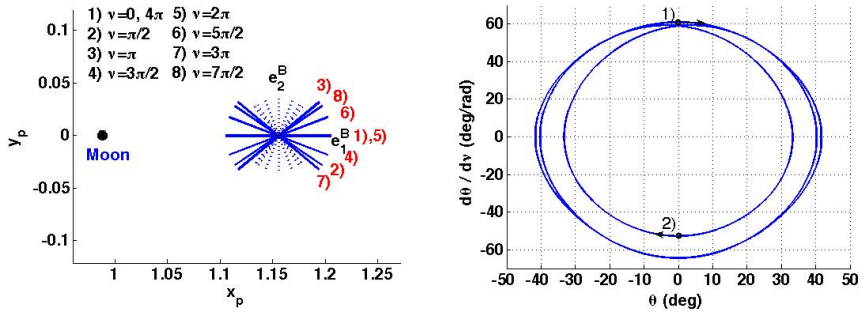

(a) $P-2$, $k_3 = 0.3$ (b) $P-2$, phase plane

Figure 21. Pitch motion of $P-2$ at L_2 in the ERTBP, $e = 0.05$

with $T = 3.358724106$ which was analyzed in Guzzetti and Howell[16] and two Lyapunov orbits around L_2 with $T = 3.47866979$ and $T = 4.187193272$. Figure 22 gives an idea of the size of the reference trajectories in the rotating frame. As an overview, the $P-1$ motion found using the cell mapping method is shown on top of the reference trajectories.

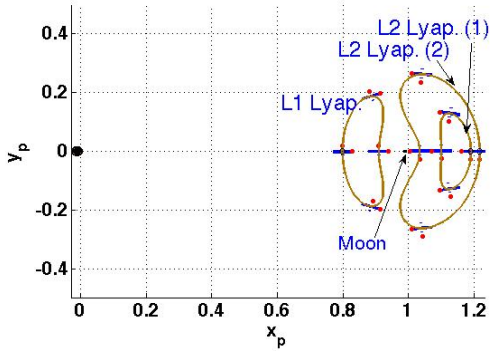

Figure 22. $P-1$ motion along reference trajectories in the rotating frame

Invariant surfaces and discrete multiple-period solutions are shown in Figures 23 to 25 for each reference trajectory. Comparing these three, the $P-1$ solution for the L_1 Lyapunov orbit has higher θ' than ones for the L_2 Lyapunov orbits. Correspondingly, pitch oscillates more in the L_1 Lyapunov orbit than the L_2 orbits as shown in Figures 23b, 24b, and 25b. One other kind of $P-1$ solution is found for the larger L_2 Lyapunov orbit. The initial pitch angle is 90 deg, which means e_2^B points to the Moon, instead of e_1^B. It is found that the two $P-1$ pitch motion solutions have reflectional symmetry with respect to $(0,0)$. Lastly, the discrete multiple-periodic period motion found using the cell mapping is shown in the phase plane in Figures 23c and 24c. All the given solutions' tolerances were able to be decreased down to $1e-5$ radians.

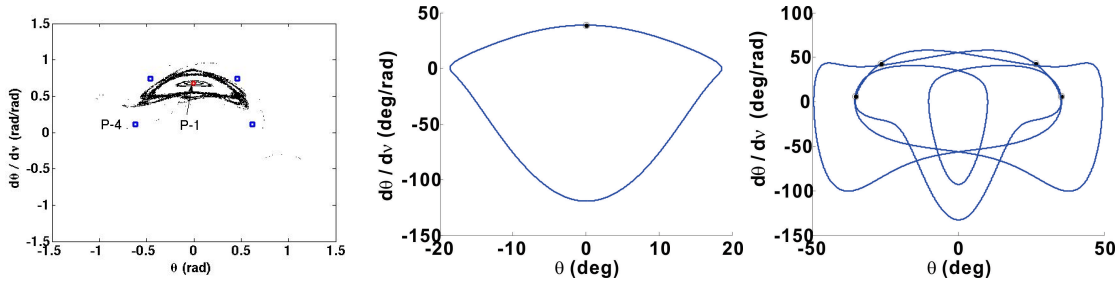

(a) Cell mapping result (b) $P-1$ (c) $P-4$

Figure 23. Pitch motion at L_1 Lyapunov orbit T=3.358724106, $k_3 = 0.4$

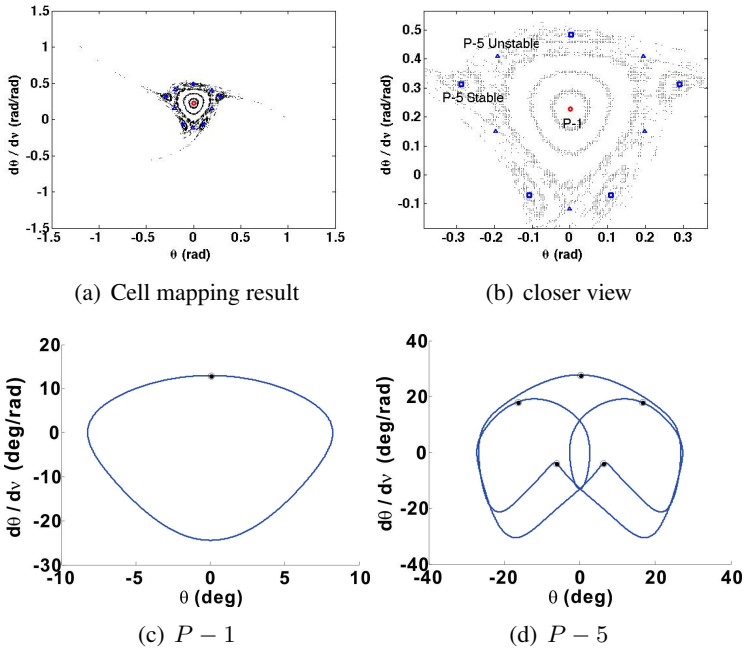

(a) Cell mapping result (b) closer view

(c) $P-1$ (d) $P-5$

Figure 24. Pitch motion at L_2 Lyapunov T=3.47866979

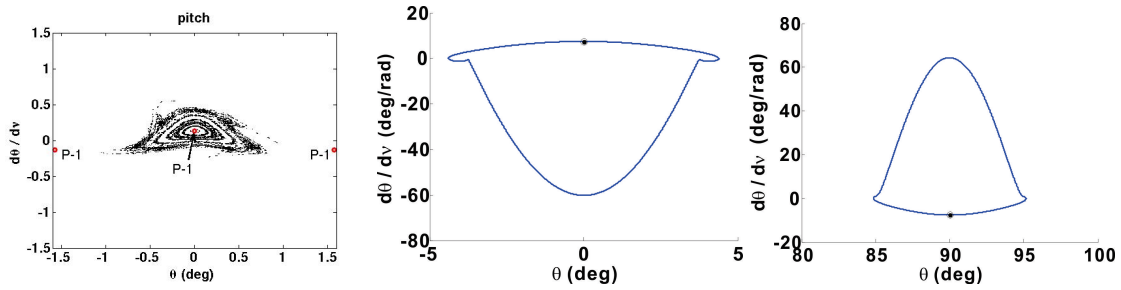

(a) Cell mapping result (b) $P-1$ (c) $P-1$

Figure 25. Pitch motion at L_2 Lyapunov T=4.187193272

ERTBP at L_4 and CRTBP reference trajectory around L_4, $k_3 = 0.1$

At L_4, as e increases, the amplitude of θ' for $P-1$ solutions increases, whereas the amplitude of $P-2$ solutions decreases. There is an isolated $P-1$ solution with $e = 0.1$, i.e., no invariant surface around the solution is found using the cell mapping. Pitch dynamics on a reference trajectory around

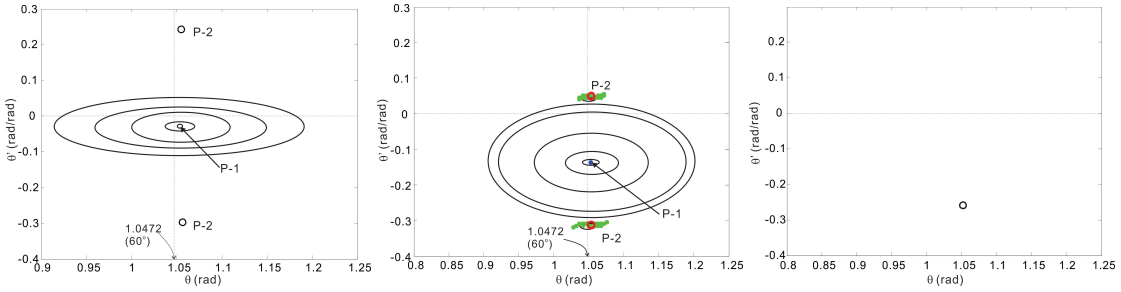

(a) $e = 0.01$ (b) $e = 0.05$ (c) $e = 0.1$

Figure 26. Cell mapping for $T = 2\pi$ at L_4 in the ERTBP, $k_3 = 0.1$

L_4 is shown in Figure 27. The period of the reference orbit in Figure 27a is $T = 6.5847782$. Figure

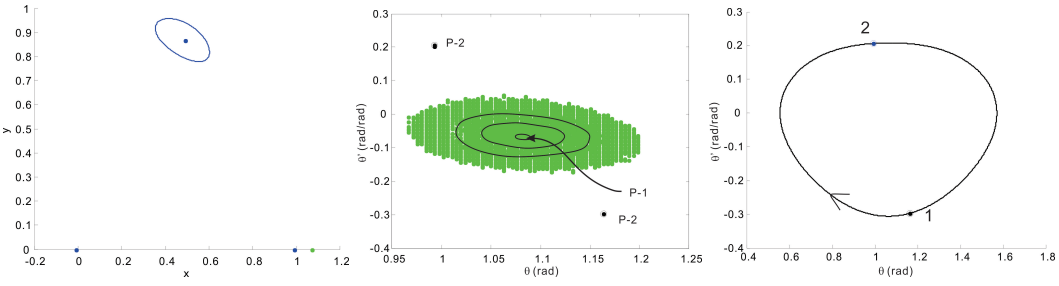

(a) Reference orbit around L_4 (b) Cell mapping result for $T = 6.5847782$ (c) Trajectory of $P-2$ solution

Figure 27. Pitch motion on an orbit around L_4, $e = 0$, $k_3 = 0.1$

27b shows the corresponding periodic solutions from the cell mapping. The center of the invariant surfaces is the $P-1$ solution. Compared to Figure 26, the periodic solutions are shifted as the reference orbit is translated. Figure 27c shows an example of the pitch motion trajectory with an initial point on the $P-2$ solution with period 2T.

CONCLUSIONS

Cell mapping methods were applied to the ERTBP to study orbit-attitude coupled solutions at the libration points and libration point orbits. The cell mapping method enabled rapid exploration across various parameters including eccentricity and the spacecraft shape. In each case the cell mapping method allowed the computation of periodic solutions including K-periodic attitude solutions and invariant surfaces which indicate quasi-periodic regions around the periodic solutions. It is demonstrated that the characteristics of pitch dynamics at L_3 in the three-body problem are close to the gravity gradient satellite in the two body problem. However, the dynamic behavior significantly changes at L_2 and L_4. Pitch oscillation of a spacecraft initially oriented to point toward the Moon grows larger, and the size of the invariant surface is reduced as eccentricity increases for both cases. In addition, a $P-1$ to $P-1$ bifurcation was found by varying the spacecraft inertia parameter at L_2. Attitude dynamics coupled with reference trajectories were also studied. Even though relatively narrow invariant surface regions were found when the spacecraft is placed at libration orbits, periodic solutions were able to be found. Multiple-periodic motions were also discovered.

FUTURE WORK

Further exploring the effects of changing eccentricity, spacecraft shape, and three-body orbits is planned. Additional work will focus on refining the cell-mapping and extended cell-mapping results even further. This process will aid in differentiating potential periodic solutions from quasi-periodic orbits.

ACKNOWLEDGEMENTS

Part of the research presented in this paper has been carried out at the Jet Propulsion Laboratory, California Institute of Technology, under a contract with the National Aeronautics and Space Administration. The High Performance Computing resources used in this investigation were provided by funding from the JPL Office of the Chief Information Officer.

REFERENCES

[1] Beletskii, V. V.: The Satellite Motion about Center of Mass. Publishing House, Science, Moscow, 1965.

[2] Modi, V. J.; Brereton, R. C.: Periodic Solutions Associated with the Gravity-Gradient-Oriented System: Part 1. Analytical and Numerical Determination. AIAA Journal, Vol. 7, No. 7, July, pp. 1217–1225, 1969.

[3] Zlatoustov, V. A.; Okhotsimsky, D. E.; Sarychev, V. A.; Torzhesky, A. P.: Investigation of a Satellite Oscillations in the Plane of an Elliptic Orbit. Applied Mechanics; proceedings of the eleventh international congress of applied mechanics, Munich (Germany), pp. 436–439, 1964.

[4] Modi, V. J.; Brereton, R. C.: Periodic Solutions Associated with the Gravity-Gradient-Oriented System: Part 2. Stability Analysis. AIAA Journal, Vol. 7, No. 7, July, pp. 1465–1468, 1969.

[5] Koh, D; Flashner, H.: Global Analysis of Gravity Gradient Satellite's Pitch Motion in an Elliptic Orbit. Journal of Computational and Nonlinear Dynamics, Vol. 10, pp. 061020-1-061020-11, 2015

[6] Farquhar, R. W. : The Flight of ISEE-3/ICE: Origins, Mission History, and a Legacy. Journal of the Astronautical Sciences, Vol. 49, No. 1, pp. 23–74, 2001.

[7] Lo, M. W.; Williams, B. G.; Bollman, W. E.; Han, D.; Hahn, Y.; Bell, J. L.; Barden, B. : Genesis mission design. Journal of the Astronautical Sciences, Vol. 49, No. 1, pp. 169–184, 2001.

[8] Dunham, D. W.; Farquhar, R. W. : Libration point mission, 1978-2002. Libration Point Orbits and Applications: Proceedings of the Conference, Aiguablava, Spain, 10-14, June, 2002.

[9] Kane, T. R.; Marsh, E. L.: Attitude stability of a symmetric satellite at the equilibrium points in the restricted three-body problem. Celestial mechanics, Vol. 4, No. 1, pp. 78-90, 1971.

[10] Robinson, W. J.: Attitude stability of a rigid body placed at an equilibrium point in the restricted problem of three bodies. Celestial Mechanics and Dynamical Astronomy Vol. 10, No. 1, 17-33, 1974.

[11] Ashenberg, J.: Satellite Pitch Dynamics in the Elliptic Problem of Three Bodies. Journal of Guidance, Control, and Dynamics, Vol. 19, no. 1, pp. 68–74, 1996.

[12] Brucker, E.; Gurfil, P.: Analysis of gravity-gradient-perturbed rotational dynamics at the collinear Lagrange points. The Journal of the Astronautical Sciences, Vol. 55, No. 3, pp. 271–291, 2007.

[13] Wong, B.; Patil, R.; Misra, A.: Attitude Dynamics of Rigid Bodies in the Vicinity of Lagrangian Points. Journal of Guidance, Control, and Dynamics, Vol. 31, pp. 252-256, 2008.

[14] Guzzetti, D.; Howell, K. C.: Coupled Orbit-Attitude Dynamics in the Three-Body Problem: a Family of Orbit-Attitude Periodic Solutions. AIAA/AAS Astrodynamics Specialist Conference, 2014

[15] Knutson, A. J.; Guzzetti, D.; Howell, K. C.: Attitude Responses in Coupled Orbit-Attitude Dynamical Model in Earth-Moon Lyapunov Orbits. Journal of Guidance, Control, and Dynamics, Vol. 38, pp. 1264–1273, 2015

[16] Guzzetti, D.; Howell, K. C.: Natural periodic orbit-attitude behaviors for rigid bodies in the three-body periodic orbits. Acta Astronautica, http://dx.doi.org/10.1016/j.actaastro.2016.06.025, 2016

[17] Hsu, C. S.: A Theory of Cell-to-Cell Mapping Dynamical Systems. J. Applied Mechanics, Vol. 47, No. 4, Dec. 931–939, 1980.

[18] Hsu, C. S.: An Unravelling Algorithm for Global Analysis of Dynamical Systems: An Application of Cell-to-Cell Mappings. J. Applied Mechanics, Vol. 47, pp. 940–948, 1980.

[19] Hsu, C. S.: A generalized theory of cell-to-cell mapping for nonlinear dynamical systems. J. Applied Mechanics, Vol. 48, No. 3, pp. 634–642, 1981.

[20] Dellnitz, M.; Junge, O.: On the Approximation of Complicated Dynamical Behavior. SIAM Journal on Numerical Analysis, Vol. 36, no. 2, 1999. 491–515.

[21] Dellnitz, M.; Froyland, G.; Junge, O.: The algorithms behind GAIO – Set oriented numerical methods for dynamical systems. Ergodic Theory, Analysis, and Efficient Simulation of Dynamical Systems, Springer, Fiedler, B. 2001. 145–174

[22] Dellnitz, M.; Junge, O.: Set Oriented Numerical Methods in Space Mission Design. Modern Astrodynamics, Elsevier Astrodynamics Series, Butterworth-Heinemann. 2006.

[23] Bollt, E. M.; Santitissadeekorn, N.: Applied and Computational Measurable Dynamics. Society for Industrial and Applied Mathematics, Philadelphia, Pennsylvania. 2013.

[24] Hughes, P. C.: Spacecraft Attitude Dynamics. John Wiley & Sons, Inc.,New York, 1986.

[25] Flashner, H.; Hsu, C. S.: A Study of Nonlinear Periodic Systems via the Point Mapping Method. International Journal for Numerical Methods in Engineering, Vol. 19, No. 2, pp. 185–215, 1983.

[26] Guttalu, R. S.; Flashner, H.: Stability Analysis of Periodic Systems by Truncated Point Mapping. Journal of Sound and Vibration, Vol. 189, No. 1, pp. 33–54, 1996.

[27] Golat, M.; Flashner, H.: A New Methodology for the Analysis of Periodic Systems. Nonlinear Dynamics, Vol. 28, No. 1, pp. 29–51, 2002.